Pulsing Techniques for Solid-Propellant Rocket Motors: Modeling and Cold-Flow Testing

Joseph D. Baum*
University of Dayton Research Institute, Dayton, Ohio
Richard L. Lovine†
Aerojet Tactical Systems, Sacramento, California
and
Jay N. Levine‡
Air Force Rocket Propulsion Laboratory, Edwards Air Force Base, California

This paper presents results obtained as part of a research program designed to develop guidelines for pulsing solid-propellant rocket motors to determine their susceptibility to finite-amplitude disturbances. The present experimental phase consisted of pulsing closed tubes filled with cold gases and motor chambers filled with hot combustion products, utilizing pyrotechnic, low brisance, and piston pulsers. Performance models were developed to calculate the mass and energy flow rates of these pulsers. An existing nonlinear combustion instability program was modified to model the effect of fore-end pulsing by imposing the calculated mass and energy flow rates as boundary conditions. A comparison of the measured and predicted pressure waves (amplitude and frequency content) in these chambers indicates very good agreement. Further validation of the pulse prediction methodology using actual pulsed solid rocket motor data is in progress.

Nomenclature

a = gas only, speed of sound
A = vent area
A_p = piston area
A_1 = chamber area
C = charge weight
C_d = orifice coefficient
c_p = isobaric heat capacity
C_s = subcritical flow correction
c_v = isochoric heat capacity
C_w = sonic flow coefficient
d_v = vent diameter
E_i = energy venting rate into the chamber
f = fraction of burning pellets remaining in pyro pulser
F = pyro pulser coefficient, RT_0
f_v = fraction vent area opened by piston travel in brisance pulser
g = gravitational constant
K = parameter defined in Eq. (5)
m = mass of gas in combustion chamber
$\dot{m}_b$ = mass burning rate of pyro charge
$\dot{m}_i$ = mass venting rate into chamber
$\dot{m}_o$ = mass flow rate out of pulser
n = charge burning rate exponent
N = number of charge pellets in chamber
p = pressure
p_b = bore pressure
p_c = motor chamber pressure
R = specific gas constant
r_v = vent radius
s = web fraction burned
$\dot{s}$ = rate of change of web fraction burned
t = time
T = gas temperature
T_i = temperature of the combustion products entering the breech
T_0 = isochoric flame temperature
u = piston velocity
u_1 = gas velocity at chamber fore end
v, v_0 = volume and initial volume, respectively
x, x_s = piston travel and total stroke, respectively
γ = isentropic constant
ρ = density

Subscripts

1 = mesh point 1 located at the fore end
$1'$ = origin of left-running characteristics reaching point 1

Presented as Paper 82-0359 at the AIAA 20th Aerospace Sciences Meeting, Orlando, Fla., Jan. 11-14, 1982; submitted Feb. 5, 1982; revision received Aug. 13, 1982. This paper is declared a work of the U.S. Government and therefore is in the public domain.

*Research Scientist; currently with the Air Force Rocket Propulsion Laboratory, Edwards AFB, Calif. Member AIAA.
†Engineering Specialist. Member AIAA.
‡Research Physical Scientist.

Introduction

NONLINEAR axial mode instabilities in solid-propellant rocket motors can be initiated by random finite-amplitude events such as the expulsion of an igniter or insulation fragment through the nozzle. Such instabilities are usually characterized by large-amplitude oscillations having steep-fronted, shock-like waveforms and are often accompanied by significant increases in mean chamber pressure. When instability is initiated in this manner in a motor that is otherwise linearly stable (i.e., stable to infinitesimal disturbances), it is said to be a "triggered" instability. The existence of triggered instabilities is a direct result of the amplitude dependence of the acoustic energy gain or loss mechanisms in a solid rocket motor, e.g., pressure- and velocity-coupled driving, nozzle and particle damping, acoustic mean flow interactions, etc. This amplitude dependence also accounts for the formation of limit cycles in which the net gains and losses are balanced. Triggering of instabilities in solid rocket motors by natural finite-amplitude pulses suggests that artificial laboratory pulsers can be used to investigate this phenomenon.

To help assure the stability of production tactical motors, the Air Force has, therefore, recently been requiring that contractors pulse prototype motors during development. If done properly, the pulse testing of solid rocket motors should virtually eliminate the unexpected occurrence of instability in solid rocket motors. However, the use of pulses that are too strong, or pulses that do not simulate natural pulsing phenomena, could easily result in the unjustified expenditure of resources to solve a problem that, in reality, did not exist. Alternatively, tests utilizing pulses that are inadvertently too weak might be no better than not testing at all. Thus, there is a need for rational pulsing guidelines directly related to the natural self-pulsing characteristics of solid rocket motors.

The concept of evaluating motor stability by pulsing has been utilized in the past to test both liquid[1] and solid propellant rocket motors.[2-6] It has been demonstrated many times that a given linearly stable motor design can be pulsed into instability. However, the physical mechanisms responsible for the pulse initiation of nonlinear instability are not yet fully understood. The influence of all of the pulse characteristics (amplitude and frequency content of the pressure and velocity waveforms) on triggering is also not completely understood at this time. The importance of properly describing the pressure and the velocity waveforms of the pulse were demonstrated theoretically in Ref. 7, wherein dramatically different motor responses were obtained for standing and traveling pulse-type disturbances. Therefore, a complete study of pulsing phenomena must include not only the characterization of the waveforms induced by both natural pulses and pulse-generating devices, but also an investigation of the response of the motor to various types of pulses. With this information, it should be possible to design pulse units that will simulate the triggering potential of natural pulsing mechanisms such as ejection of inert materials through the nozzle.

A previous investigation of pulsing criteria for solid rocket motors[6] yielded a semiempirical model that was limited to predicting the maximum initial pressure amplitude of the pulse. No attempt was made to predict the pulse waveform and pulse velocity or to couple this model with a stability analysis of the motor itself. This investigation is the first attempt to predict, a priori, all of the pulse characteristics generated by several types of laboratory pulser units. Moreover, this investigation is the first attempt to combine the pulser performance models with a nonlinear combustion instability analysis of the motor.

The development of ballistic models for three different pulsers (pyrotechnic, piston, and reduced brisance) was the first step in the overall model development. Ballistic analysis of the pulser design provides the mass and energy fluxes that are injected into the motor. A nonlinear combustion instability program[8] that solves the partial differential equations governing the associated flow and combustion in solid-propellant rocket motors was then modified to model the effect of fore end pulsing based on the mass and energy flux data provided by the pulser ballistic analysis. Combining these models allows a priori predictions of both the injected pulse and the combustion response to this pulse to be performed.

In order to examine the validity of the pulse prediction models, experiments were conducted in which closed tubes filled with cold nitrogen and helium and motors filled with hot combustion products were pulsed by the three different pulsers. Predicted and measured pulse amplitudes and waveforms were then compared. The pulser performance models, the modifications made to couple these models to the chamber analysis, and a comparison of predicted and experimentally measured pulse waveforms are reported in this paper.

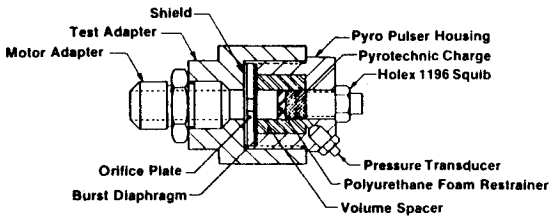

Fig. 1 Schematic of the pyro pulser unit.

Pulser Performance Models

Three different types of laboratory pulsers were employed in the present study: the pyro, piston, and low-brisance pulsers. Only a brief overview of their design and operation is given here. Further details are given in Ref. 9.

Pyrotechnic Pulser

A schematic of the pyro pulser is shown in Fig. 1. A squib initiator ignites a pyrotechnic charge (Red Dot double-base powder) in the combustion chamber. The gaseous combustion products increase the pressure in the chamber to the rupture pressure of the burst diaphragm. As the diaphragm bursts, the combustion products plus a fraction of the remaining unburned pyrotechnic charge expand into the pulser barrel and are then vented into the chamber. A typical pressure history obtained with the pyro pulser is shown in Fig. 2. With this pulser the mass and energy flux rates reach a maximum value in a fraction of a millisecond after the diaphragm bursts and then decay in an approximately exponential manner as the combustion products are vented into the chamber. The pulser is typically designed to provide a vent time of approximately 20% of the period of the fundamental acoustic mode of the chamber. By varying the design of the pulser, it is possible to control the venting time. The main features of the pulse produced by this pyro pulser are a very fast rise in the pressure and mass flow rate up to a predetermined maximum value followed by an exponential decay with a controllable decay rate.

Performance analysis of the pyro pulser is posed as a simple lumped volume venting problem, neglecting dynamic effects. The analysis is based on the solution of the bulk mass and energy balances as applied to the pulser combustion chamber. Since the pressure ratio across the vent is very high, the vent can be assumed to be choked during most of the injection period. The pulser model also assumes that the back pressure (chamber pressure) does not increase significantly. Thus, it is possible to uncouple the pulser ballistics from the chamber flowfield solution, even for the short time at the end of the injection during which the vent is not choked.

The conservation equations to be solved are

Mass

$$\frac{dm}{dt} = \dot{m}_b - \dot{m}_o \tag{1}$$

Energy

$$\frac{dc_v Tm}{dt} = c_v T_0 \dot{m}_b - c_p T \dot{m}_o \tag{2}$$

The mass flow rate through the vent is

$$m_o = C_s C_d C_w A p / (T/T_0)^{1/2} \tag{3}$$

where

$$C_s = K\left(\frac{p_c}{p}\right)^{1/\gamma}\left[1-\left(\frac{p_c}{p}\right)^{(\gamma-1)/\gamma}\right]^{1/2}, \frac{p_c}{p} > \left(\frac{2}{\gamma+1}\right)^{\gamma/(\gamma-1)}$$

$$= 1, \frac{p_c}{p} < \left(\frac{2}{\gamma+1}\right)^{\gamma/(\gamma-1)} \tag{4}$$

$$K = \left(\frac{2}{\gamma-1}\right)^{1/2}\left(\frac{\gamma+1}{2}\right)^{(\gamma+1)/2(\gamma-1)} \tag{5}$$

and

$$C_w = \left(\frac{g\gamma}{F}\right)^{1/2}\left(\frac{2}{\gamma+1}\right)^{(\gamma+1)/2(\gamma-1)} \tag{6}$$

The coefficient C_s provides the mass flow reduction due to subsonic flow, while C_w is the sonic flow coefficient. Using the equation of state for a perfect gas, the mass and energy balances can be manipulated to form the following set of ordinary differential equations:

$$\frac{dT}{dt} = \left[fC\dot{s}\left(1-\frac{T}{T_0}\right) - (\gamma-1)\left(\frac{T}{T_0}\right)^{1/2} C'_w A p\right]\frac{T}{pv/F} \tag{7}$$

$$\frac{dp}{dt} = \left[fC\dot{s} - \gamma\left(\frac{T}{T_0}\right)^{1/2} C'_w A p\right]\frac{F}{v} \tag{8}$$

where

$$C'_w = C_s C_d C_w \tag{9}$$

Solution of this set of equations with initial conditions (pressure, temperature, and fraction of charge consumed evaluated at the time the burst disk fails) yields the output mass flux $\dot{m}_o$ and energy flow rate $\dot{m}_o c_p T$. These values are utilized as fore end boundary conditions for the chamber flow model.

Low-Brisance Pulser

When pulsing solid-propellant rocket motors for qualification purposes, simulation of natural motor pulsing phenomena is desirable. For this purpose, a pulser with longer rise and decay times that simulates ejection of inert material through the nozzle is desirable. Pulses with similar characteristics can be produced with ejecta pulsers[6] that eject inert plugs into the motor. Nevertheless, since it is not always possible to use ejecta pulsers with real motors, an alternative device called the low-brisance pulser was developed. This device utilizes a variable vent area to increase the rise time of the pulse. A schematic of the low-brisance pulser is shown in Fig. 3. Upon firing of the pyrotechnic charge and burst of the rupture disk, the pressure generated by the expanding combustion products acts on the piston base. The piston is driven back and the vent begins to open. As the piston traverses the vent opening, the mass flux into the motor increases exponentially from zero to a maximum value and then decays back to zero. A typical performance curve for the low-brisance pulser is shown in Fig. 4. Both the mass injection rate and its rise time can be controlled by varying the parameters which affect the piston velocity. Calculation of the mass and energy flow rates for this pulser design is based upon the bulk balance of mass and energy in the chamber and a force balance on the piston. Mass and energy conservation equations are given, respectively, as

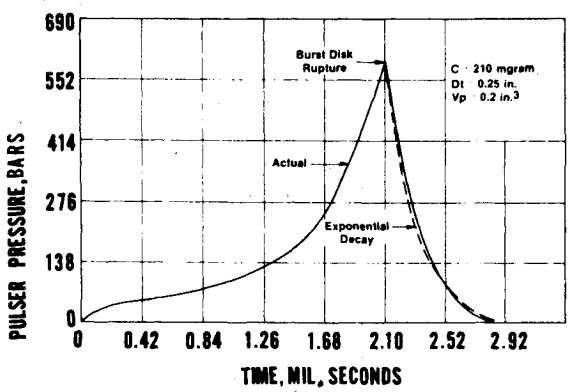

Fig. 2 Pyro pulser pressure-time function.

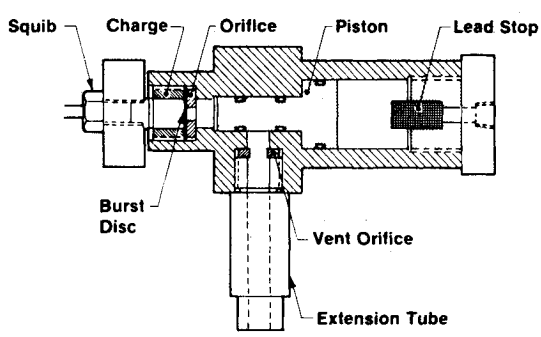

Fig. 3 Schematic of the low-brisance unit.

$$\frac{dm}{dt} = \dot{m}_i - \dot{m}_o \tag{10}$$

$$\frac{dc_v Tm}{dt} = c_p T_i \dot{m}_i - c_p T \dot{m}_o - pA_p u \tag{11}$$

The mass and energy flow rates into the breech, $\dot{m}_i$ and $\dot{m}_i c_p T_i$, are equal to the corresponding flow rates out of the charge holder. The ballistic performance of the charge holder is identical to that of the pyro pulser. The mass and energy flow rates out of the pulser (into the motor port), $\dot{m}_o$ and $\dot{m}_o c_p T$, depend on the amount of vent area exposed by the moving piston. The equation describing the mass flow rate through the vent is similar to the one obtained with the pyro pulser, but with an added multiplying factor f_v which represents the fraction of vent area uncovered by the moving piston,

$$\dot{m}_o = f_v C_s C_d C_w A p/(T/T_0)^{1/2} \tag{12}$$

Let x_v be the distance the piston must travel before the edge of the vent is reached, x the distance traveled, and d_v the vent diameter. Then,

$$\begin{aligned} f_v &= 0, x < x_v \\ &= 1/2 + (1/\pi)\left[y\sqrt{1-y^2} + \tan^{-1}\left(y/\sqrt{1-y^2}\right)\right], 0 < x - x_v < d_v \\ &= 1, x - x_v > d_v \end{aligned} \tag{13}$$

where

$$y = [(x - x_v)/r_v] - 1 \tag{14}$$

Manipulation of the mass and energy balances results in the following set of ordinary differential equations having pressure and temperature as dependent variables:

$$(v_0 + A_p x)\frac{dp}{dt} = \gamma R T_i \dot{m}_i - \gamma R T \dot{m}_o - \gamma p A_p u \tag{15}$$

$$\frac{1}{T}\frac{dT}{dt} = \frac{[(\gamma T_i/T) - 1]RT\dot{m}_i - (\gamma-1)RT\dot{m}_o - (\gamma-1)pA_p u}{p(v_0 + A_p x)} \tag{16}$$

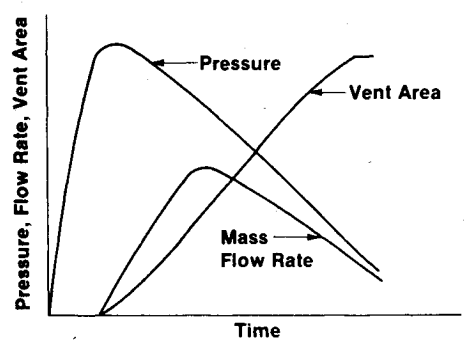

Fig. 4 Low-brisance pressure-time function.

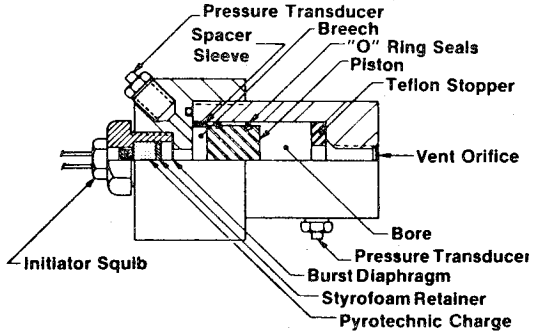

Fig. 5 Schematic of the piston pulser unit.

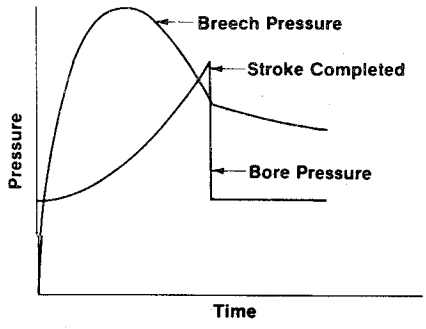

Fig. 6 Piston pulser pressure-time function.

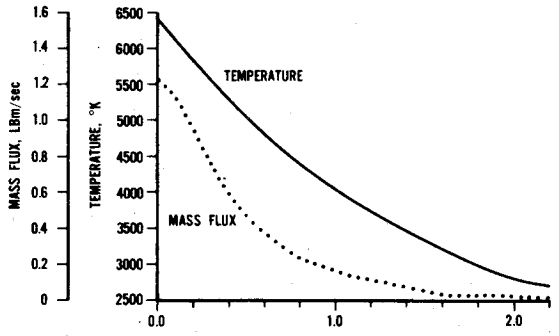

Fig. 7a Pyro pulser calculated performance.

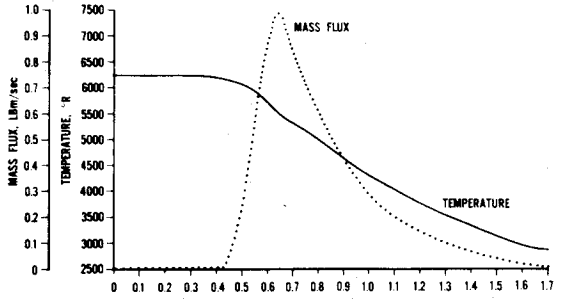

Fig. 7b Low-brisance calculated performance.

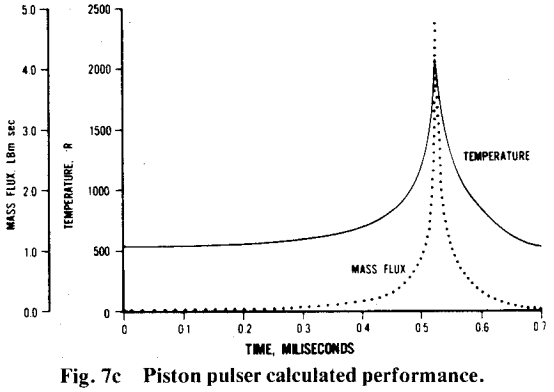

Fig. 7c Piston pulser calculated performance.

Piston Pulser

In order to allow for even more variation in the range of pulse characteristics available for motor test and research purposes, another type of pulser called the piston pulser was designed. A schematic of the piston pulser is shown in Fig. 5. After rupture of the burst diaphragm, the combustion gases and the unburned fraction of the charge enter the breech volume. As the pressure increases, the piston accelerates into the bore volume. The gases in the bore are compressed by the piston and are vented into the motor. An idealized performance curve for the piston pulser is shown in Fig. 6. In reality, the pressure decay from the maximum amplitude to chamber pressure is not a discontinuous jump, but rather a rapid decay. The reason is that when the piston stops, the venting of the gases left in the vent volume takes a finite amount of time. With the piston pulser the mass and energy flow rates increase exponentially with time and decay rapidly. This is in contrast to the exponential decay only that is observed with the pyro pulser, and the significantly (typically) slower rise and decay periods observed with the reduced-brisance pulser. The piston pulser rise time and mass flow rate can be controlled by varying the breech charge or volume, the piston weight or stroke and the vent area. Since the volume of the piston pulser is in practice limited, the amount of mass that can be injected into a motor is relatively small. Thus, in order to produce relatively high-amplitude pulses, the piston pulser must be designed with very short rise and decay times. This produces a very brisant blip-like pulse.

Mass and energy injection rates are evaluated from conservation of mass and energy and a force balance on the piston. Since mass is not expelled, the breech mass balance is trivial. Conservation of the energy in the breech is

$$\frac{\mathrm{d}c_v Tm}{\mathrm{d}t} = c_v T_0 \dot{m}_b - pA_p u \tag{17}$$

Conservation of mass and energy in the bore are written, correspondingly, as

$$\frac{\mathrm{d}m}{\mathrm{d}t} = -\dot{m}_o \tag{18}$$

$$\frac{\mathrm{d}c_v Tm}{\mathrm{d}t} = p_b A_p u - c_p T_f \dot{m}_o \tag{19}$$

Finally, a force balance on the piston yields

$$m\frac{\mathrm{d}u}{\mathrm{d}t} = A(p - p_b) \tag{20}$$

The initial pressure in the breech is the rupture pressure of the burst disk. Initial conditions in the bore are identical to the initial conditions in the chamber.

Chamber Model

As previously mentioned in the introduction, a priori prediction of pulse characteristics and the combustion response to this pulse requires coupling of the pulser performance model to a chamber flowfield and combustion model. In order to achieve this coupling, an existing nonlinear combustion instability model that solves the partial differential equations that govern two-phase flow in variable cross-sectional area solid-propellant rocket motors[8] was modified to accept the pulser mass and energy flow rates as boundary conditions. Another modification of the original program was the incorporation of an improved finite-difference integration technique[7] that combines the Lax-Wendroff,[10] hybrid,[11] and artificial compression[12] schemes.

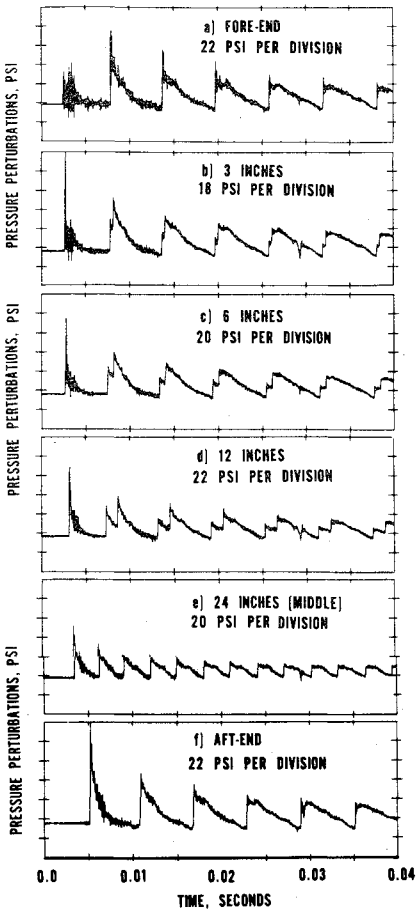

Fig. 8 Pyro pulser: time evolution of measured pressure perturbations at several locations along the chamber.

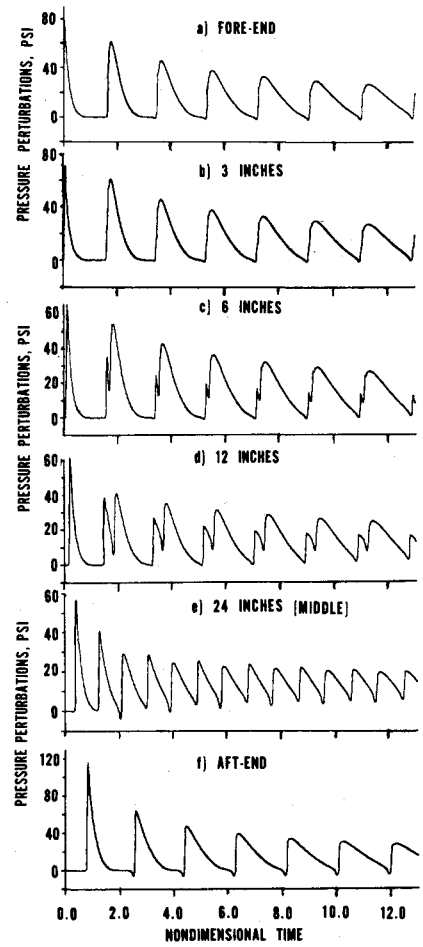

Fig. 9 Pyro pulser: time evolution of predicted pressure perturbations at several locations along the chamber.

The modified model is capable of accurately calculating the propagation of multiple steep-fronted, shock-type waves in a rocket motor, while describing each shock as a sharp nonoscillatory discontinuity. The spurious pre- and postshock oscillations that were generated by old numerical schemes (such as Rubin and Burstein,[13] MacCormack,[14] etc.), which could falsely trigger combustion instabilities, have been eliminated. The new finite-difference integration scheme is employed at all interior mesh points while the method of characteristics is employed at boundaries.

The capability to treat velocity-coupled combustion instability and to spectrally analyze the computed waveforms has also been incorporated into the instability program.[15]

The flowfield created by injection of pulser gases into a motor resembles an underexpanded plume until such time when the gases (or the pressure waves created by injection) reach the walls of the chamber. The flowfield is two-dimensional and strong mixing will take place within a few orifice diameters downstream of the pulser exit. Rather than attempt to model this complex problem, the present work sought to determine if, by the use of judicious engineering approximations, a simple one-dimensional model of the problem could yield reasonably accurate and useful results.

When developing a one-dimensional model for the solution of this problem, one has to resolve the problem of specifying the boundary conditions at the fore end and the problem of mixing between the pulser and chamber gases. Since the flow out of the pulser is supersonic (during most of the pulsing period with the pyro and low-brisance pulsers and during the interval when most of the mass is expelled from the piston pulser), the flow variables at the pulser exit are completely dependent upon conditions inside the pulser. Nevertheless, most of the fore end is a hard wall at which the gas axial velocity is zero. This head-end velocity discontinuity cannot be treated properly with a one-dimensional model, so additional approximations had to be made. Since the pulser orifice is usually very small relative to the chamber diameter, and since the velocity difference between the injected pulser gases and the chamber gases is large, mixing should rapidly reduce the velocity of the gases to a subsonic level. Based on these considerations, the following simplified model was developed. During the pulsing period the pulser mass and energy flow rates, as predicted by the pulser performance models, are specified as boundary conditions. When the pulser flow stops, the boundary treatment reverts back to the normal treatment for a hard wall. Mixing per se was not modeled, but its presence was implicitly accounted for by assuming that the pulser gases become subsonic in the process of instantaneously expanding to fill the head end of the chamber.

The equations representing this model are

$$\dot{m}_l = \rho_l u_l A_l \tag{21}$$

$$\dot{E}_l = \dot{m}_l (c_p T_l + \tfrac{1}{2} u_l^2) \tag{22}$$

$$p_l = \rho_l R T_l \tag{23}$$

$$p_l = p_{l'} + \rho_{l'} a_{l'} \gamma (u_l - u_{l'}) \tag{24}$$

Comparison of Experimental and Analytical Results

The experimental results presented in Figs. 7, 8, 10a, 11 and 13a were obtained by pulsing a closed cylindrical chamber having a length of 1.22 m (48 in.) and an internal diameter of 0.077 m (3.056 in.). The chamber was filled with nitrogen at room temperature pressurized to 100 psi chamber pressure.

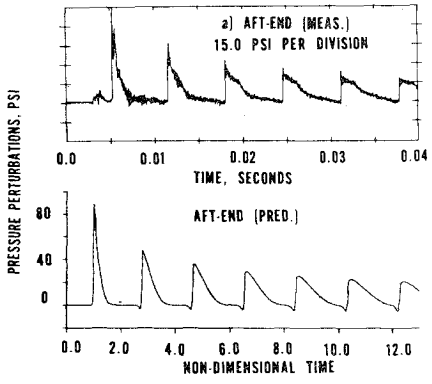

Fig. 10 Low-brisance pulser: comparison of measured and predicted pressure perturbations at the aft end.

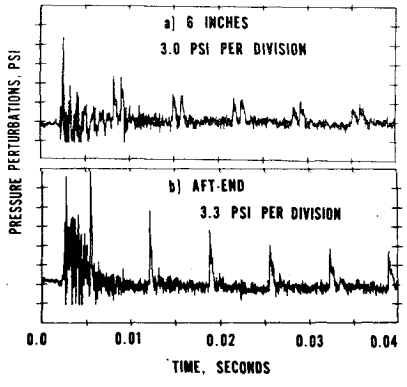

Fig. 11 Piston pulser: time evolution of measured pressure oscillations at two locations in the chamber.

By utilizing chambers filled with inert gases the characteristics of the different pulses and the resulting waveforms in the chamber can be better analyzed and understood since the complex interactions between the pulser-induced waves and the propellant combustion are eliminated. In addition, by conducting experiments with an empty chamber, it is possible to obtain data at several axial locations. This results in a more complete description of the propagating wave which, in turn, enables better understanding of wave propagation, wave steepening, and viscous losses. In this series of tests, the chamber was instrumented with six high frequency pressure transducers mounted on the sidewalls at 3, 6, 12, and 24 in. from the pulsed end and on both end closures. The pulser units were attached at the fore end of the chamber.

Performance analyses of the pyro, low-brisance, and piston pulsers yielded the temperature and mass flow rate curves that are shown in Figs. 7a-7c, respectively. The data shown in these curves indicates that the pulser units performed as expected. The time evolution of the pressure oscillations (where time is nondimensionalized by multiplying dimensional time by the sound speed divided by the chamber length) initiated in the chamber by the pyro, low-brisance, and piston pulsers are shown in Figs. 8, 10a and 11, respectively. The very short rise and decay periods of the pulse initiated by the low-brisance pulser (shown in Fig. 10a) is a result of the low back pressure (in the chamber) acting on the piston surface. Thus, in this case, the pulse and the resulting wave in the chamber are very similar to those generated by the pyro pulser. The wave is already fully shocked after propagating only 3 in. into the chamber. The pressure oscillations excited by the piston pulser (Fig. 11) feature a very fast rise and decay (similar to the pulse pressure and mass flux variation). The total mass injected by the piston pulser is small compared to the total mass in the chamber (about 0.3%). The relatively large amplitude of the resulting pressure oscillations in the chamber is due to the fact that most of the mass in the piston bore is injected into the chamber in a very short time.

Table 1 Comparison of measured and predicted maximum pressure amplitude values (psi) at the aft end

	Pyro		Low brisance		Piston	
Cycle	Measured	Predicted	Measured	Predicted	Measured	Predicted
1	112.0	118.2	75.2	88.48	20.4	15.16
2	59.9	64.7	48.0	47.68	12.5	12.51
3	46.8	47.62	36.0	36.36	9.6	11.47
4	38.9	39.38	27.5	29.78	7.6	10.8

Time evolution of pressure oscillations in the chamber, obtained by utilizing the predicted mass and energy flow rates as boundary conditions for the nonlinear combustion instability program, are shown in Figs. 9, 10b, and 12 for the pyro, low-brisance, and piston pulsers, respectively. Very good agreement between the measured and predicted waveforms (amplitude and shape) is demonstrated. Table 1 shows a comparison of the measured and predicted maximum pressure amplitude values at the aft end for the first four wave periods. Excellent agreement is demonstrated. The fact that a simplified one-dimensional model could accurately predict the wave amplitude, shape and decay rate for the first four or five cycles was somewhat surprising, but also very satisfying. The one-dimensional inviscid model does not account for viscous losses at the walls of the chamber; thus, the predicted decay rates were not expected to match the measured decay rates. The excellent agreement with measured decay rates for the first few cycles results from the fact that the initially high decay rates are primarily due to entropy increase resulting from repetitive shock-wave processing of the gas in the chamber. During this time interval, viscous wall losses are a relatively insignificant part of the total loses. The capability of the present model to predict entropy increase and waveform decay rates that are in excellent agreement with closed-form analytical results has been demonstrated in the past for several test cases.[7] Nevertheless, as expected, results obtained with this inviscid model do not match the experimental decay rates at later times, when viscous wall losses become the major loss mechanism.

A second series of cold-flow tests was conducted using helium instead of nitrogen under otherwise identical conditions. Again, excellent agreement was demonstrated between the measured and predicted waveforms.

When hot gases are injected into a cold chamber (cold-gas tests with the pyro and low-brisance pulsers), a large temperature gradient is formed near the fore end. This temperature gradient results in partial reflection of the shock returning from the aft end which, in turn, results in pressure waves that are not as steep-fronted as those predicted at the aft end. In addition, the development of a slight expansion in front of the shock can also be observed (as shown in Fig. 13). These phenomena are observed in both the measured and predicted data. In the experiment, convection, conduction, and mixing rapidly reduce the temperature gradient. The current analysis does not treat mixing or heat conduction, thus, convection is the only operative heat-transfer mechanism. Since convection is a slow process (due to the low velocity of the gases), the calculated temperature gradient remains unrealistically steep for a relatively long period of time. This results in predicted maximum fore end pressure amplitudes that are lower than the measured data. The predicted results at the center of the tube (Fig. 9e) show the marked difference between waves reflected from the fore end and waves reflected from the aft end. This temperature gradient phenomenon should not affect the predicted results when solid rocket motors are pulsed, since both the injected pulser gases and the combustion products in the chamber are at approximately the same temperature.

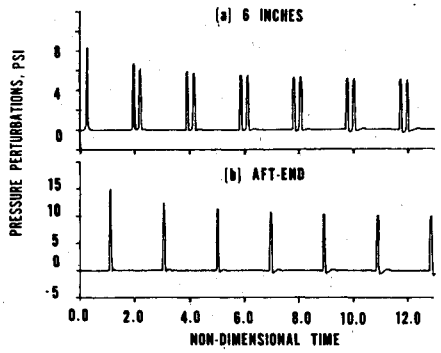

Fig. 12 Piston pulser: time evolution of predicted pressure oscillations at two locations in the chamber.

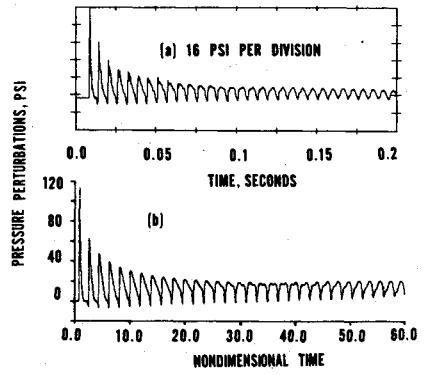

Fig. 13 Pyro pulser: comparison of measured and predicted pressure oscillations at the aft end of the chamber.

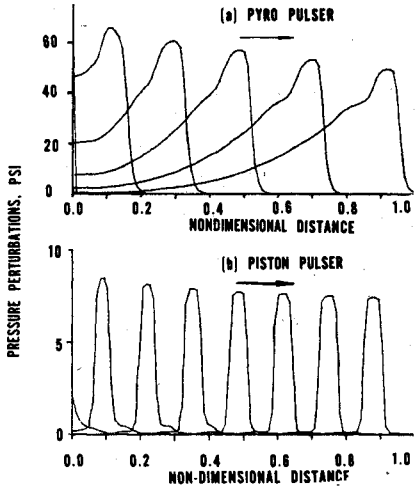

Fig. 14 Spatial evolution of pressure waves in the chamber initiated by the pyro and piston pulsers.

An additional point should be made concerning the performance analysis of the piston pulser. The piston (driven into the bore by the high pressure in the breech volume) is stopped by a Teflon stopper located at the aft end of the bore volume. The compression of the Teflon stopper has to be accounted for since the pressure and mass injection rates are rapidly increasing as the piston completes its stroke. Because the remaining volume occupied by gases at that time is small, a relatively small error in estimating the final compression distance of the Teflon stopper (referred to herein as stand-off distance) can result in a relatively large error in the predicted maximum amplitude value of the wave initiated in the chamber.

The predictions presented for the piston pulser (Fig. 12) were obtained utilizing a stand-off distance of 0.0375 in. The

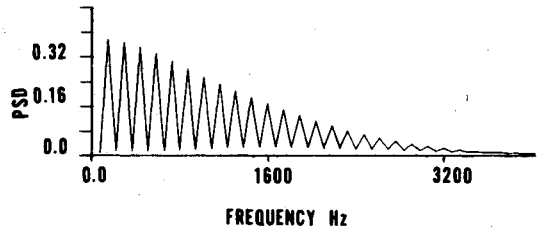

Fig. 15 Piston pulser: PSD as a function of frequency at the fore end.

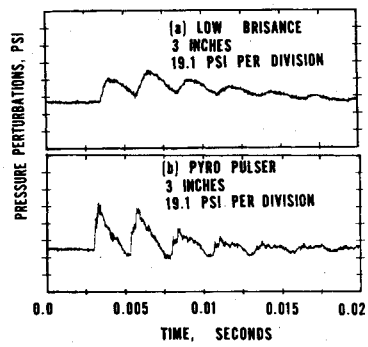

Fig. 16 Hot-flow tests: comparison of measured pressure oscillations obtained with the low-brisance and pyro pulsers.

predicted pressure results remain qualitatively the same for different stand-off distances; nevertheless, there are quantitative changes. For instance, the maximum amplitude of the first incident wave at the aft end is 8 psi with a stand-off distance of 0.10 in., 10 psi with a stand-off distance of 0.05 in., and 15 psi with a stand-off distance of 0.0375 in. Thus, previous knowledge of the stand-off distance is needed for accurate prediction of the pulse amplitude produced by the piston pulser.

Spatial evolution of pressure waves in the first half wave period, as initiated in the chamber by the pyro and piston pulsers, are shown in Figs. 14a and 14b, respectively. The differences between these pulses are evident in the figures. The very fast rise and decay times of the pulse generated by the piston pulser result in a very narrow steep-fronted and steep-backed wave. The prediction of such waveforms in a sharp nonoscillatory manner is a formidable test of a numerical scheme. The ability of the present numerical technique to reproduce these waves with only slight postexpansion oscillations is another indication of the excellence of this shock-capturing technique for all types of wave propagation problems. Spectral analysis of the very narrow wave predicted for the piston pulser (results at the fore end are shown in Fig. 15) indicates a very high percentage of energy in the higher modes. This result is significantly different from spectral analysis results obtained for a steep-fronted, shocked waveform[7] for which the energy contained in the higher modes falls as $1/n^2$ with respect to the energy contained in the fundamental mode (where n is the mode number).

A second series of experiments was conducted recently utilizing a 1.22 m (48 in.) long, 0.038 m (1.5 in.) i.d. chamber filled with hot combustion products. A subsonic vent was utilized to maintain a constant pressure of 1000 psi. The chamber was instrumented with six high-frequency Kistler pressure transducers. The transducer locations were the same as used in the cold-flow experiments. The pyro, low-brisance, and piston pulsers were utilized to pulse the chamber at the head end. The total mass discharged from each pulser was held constant, with a ratio of mass injected to mass in the chamber of 0.005.

The characteristics of the resulting pressure waves in the chamber obtained with the pyro and piston pulsers are, in general, similar to those obtained in the cold-flow series of

tests. The low-brisance pulser results were, however, significantly different. In the cold-flow tests, the back pressure acting on the piston was too low, resulting in a rise time that was too short and a pulse shape very similar to that generated by the pyro pulser. In the hot-gas tests, the back pressure is high and a much slower rise time was obtained. The resulting pressure wave in the chamber (shown in Fig. 16a) is significantly different from the wave generated by the pyro pulser (Fig. 16b). The wave generated by the pyro pulser is already fully shocked after propagating 3 in. into the chamber. In contrast, the wave generated by the low-brisance pulser is steep but never fully shocked and the transition to a sinusoidal-type waveform is faster. Although the total mass injected by the pulsers was identical, the pressure amplitudes of the waves generated are a strong function of the mass injection rate, a faster injection yielding higher amplitudes. The maximum amplitude of the first reflected pressure wave at the fore end generated by the piston pulser was 111 psi, compared to 52 psi for the pyro pulser and 32 psi with the low-brisance pulser.

The hot-gas test results were obtained only recently. Comparison of theoretically predicted results and the experimental data is currently in progress.

Conclusions

Based on the results obtained in this investigation, it was concluded that the original objective of developing a simple model capable of the accurate, a priori prediction of mass and energy flow rates produced by three different types of laboratory pulsers, and the waveforms produced by these pulsers inside a chamber, was achieved.

Ballistic models of the pyro, low-brisance, and piston pulsers were developed utilizing a simple lumped volume treatment. The mass and energy flow rates calculated using these pulser performance models are utilized as boundary conditions for the chamber flow problem, which is solved using a modified nonlinear combustion instability model. The ability of the combined pulser/chamber flow models to predict the pulsed waveforms (amplitude and harmonic content) in a closed chamber filled with cold gases (nitrogen and helium) was demonstrated in this paper. Excellent agreement between the measured and predicted pressure waves in the chamber was demonstrated even though a simple one-dimensional inviscid analysis was utilized to model a complex two-dimensional viscous process.

Both the experimental and analytical results demonstrate that the pulse characteristics are primarily governed by the mass flux rate from the pulser into the chamber. The pulse waveform was very similar to the shape of the respective pulser mass flux curves for each of the three types of pulsers tested.

The general applicability of the present pulsing model should be subject to further examination by comparing predictions and experimental data over a wider range of conditions than presented herein, especially for higher chamber pressures and under actual motor firing conditions.

Finally, the combination of the performance analysis of the pulser and the nonlinear combustion instability model should yield a capability to predict, a priori, pulse-triggered instability phenomenon in solid rocket motors. The accuracy of these predictions may be inhibited by present deficiencies in combustion response modeling. Good experimental data for both pressure-coupled and velocity-coupled response functions over a wide frequency range, if available, could be used to alleviate this deficiency.

Acknowledgment

This work was partially supported under Air Force Contract F04611-81-C-0012.

References

[1] Combs, L.P. et al., "Improvement of Bombs and Pulse Guns as Combustion Stability Ratings Devices," AFRPL-TR-68018, March 1968.

[2] Dickinson, L.A., "Command Initiation of Finite Wave Axial Combustion Instability in Solid Propellant Rocket Motors," *ARS Journal,* Vol. 32, March 1962, pp. 643-644.

[3] Roberts, A.K., "Development of the 9K11000 Black Brant III Rocket Engine," *CAS Journal,* June 1962, pp. 137-143.

[4] Morris, E.P., "A Pulse Technique for the Evaluation of Combustion Instability in Solid Propellant Rocket Motors," *CAS Journal,* 1965, pp. 329-333.

[5] Brownlee, W.G., "Nonlinear Axial Combustion Instability in Solid Propellant Motors," *AIAA Journal,* Vol. 2, Feb. 1964, pp. 275-284.

[6] Murray, J.A., Condon, J.A., and Krusch, D.E., "Pulsing Criteria for Solid Rocket Motors," Vol. I, Final Report, and Vol. II, "Motor Pulsing Design Manual," AFRPL-TR-79-45, 1980.

[7] Baum, J.D. and Levine, J.N., "Numerical Techniques for Solving Nonlinear Instability Problems in Solid Rocket Motors," *AIAA Journal,* Vol. 20, July 1982, pp. 955-961.

[8] Levine, J.N. and Culick, F.E.C., "Nonlinear Analysis of Solid Rocket Combustion Instability," AFRPL TR-74-45, Oct. 1974.

[9] Lovine, R.L., "Nonlinear Stability for Tactical Motors-Pulsing Consideration," Paper presented at 18th JANNAF Combustion Meeting, Pasadena, Calif., Oct. 1981.

[10] Lax, P.D. and Wendroff, B., "System of Conservation Laws," *Communications on Pure and Applied Mathematics,* Vol. 13, 1960, pp. 217-237.

[11] Harten, A. and Zwas, G., "Self Adjusting Hybrid Schemes for Shock Computations," *Journal of Computational Physics,* Vol. 9, 1972, pp. 568-583.

[12] Harten, A., "The Artificial Compression Method for Computation of Shocks and Contact Discontinuities: III, Self Adjusting Hybrid Schemes," AFOSR TR-77-0659, March 1977.

[13] Rubin, E.L. and Burstein, S.Z., "Difference Methods for the Inviscid and Viscous Equations of a Compressible Gas," *Journal of Computational Physics,* Vol. 2, 1967, pp. 178-196.

[14] MacCormack, R.W., "Proceedings of the Second International Conference on Numerical Methods in Fluid Dynamics," *Lecture Notes in Physics,* Vol. 8, edited by M. Holt, Springer-Verlag, New York, 1971, pp. 151-163.

[15] Levine, J.N. and Baum, J.D., "A Numerical Study of Nonlinear Instability Phenomena in Solid Rocket Motors," AIAA Paper 81-1524, July 1981.